Sensor Development for Liquid Water Detection in Dry Storage Casks: FY 2023 Status

Spent Fuel and Waste Disposition

Prepared for U.S. Department of Energy Spent Fuel and Waste Science and Technology James Fitzpatrick, Naveen Karri, Ryan M. Meyer

> September 8, 2023 M3SF-23PN010203027 PNNL- 34794

DISCLAIMER

This information was prepared as an account of work sponsored by an agency of the U.S. Government. Neither the U.S. Government nor any agency thereof, nor any of their employees, makes any warranty, expressed or implied, or assumes any legal liability or responsibility for the accuracy, completeness, or usefulness, of any information, apparatus, product, or process disclosed, or represents that its use would not infringe privately owned rights. References herein to any specific commercial product, process, or service by trade name, trademark, manufacturer, or otherwise, does not necessarily constitute or imply its endorsement, recommendation, or favoring by the U.S. Government or any agency thereof. The views and opinions of authors expressed herein do not necessarily state or reflect those of the U.S. Government or any agency thereof.

Contents

1.	INTI	INTRODUCTION			
	1.1	Sensing Approach	2		
	1.2	Report Contents and Organization			
2.	FINI	ITE ELEMENT MODEL DESCRIPTION	5		
	2.1	Geometry	5		
	2.2	Material Properties	6		
3.	LOA	LOADS AND BOUNDARY CONDITIONS			
	3.1	Implicit Pre-Load Analysis	7		
	3.2	Damped Transient Analysis	7		
	3.3	Guided Wave Transient Analysis	9		
4.	RESULTS				
5.	SUMMARY, CONCLUSIONS, AND FUTURE EFFORTS				
6.	REFERENCES				

List of Figures

Figure 1.	Depiction of a nominal baseplate component with excitation applied at the 0° location on the baseplate circumference.	2
Figure 2.	Dispersion curves for group velocities of antisymmetric and symmetric modes	3
Figure 3.	Wave modes in the wall under symmetric and antisymmetric excitation	3
Figure 4.	Cask Canister Geometry	5
Figure 5.	Undamped Transient Analysis Post-Preload	8
Figure 6.	Damping Application Time History	8
Figure 7.	System Rigid Body Displacement	9
Figure 8.	Input Excitation Signal	9
Figure 9.	Signal Time History at 0°-90°-180° Locations: X Component of Velocity	11
Figure 10.	Signal Time History at 0°-90°-180° Locations: Y Component of Velocity	12
Figure 11.	Signal Time History at 0°-90°-180° Locations: Z Component of Velocity	12
Figure 12.	Surface Amplitude: X Component of Velocity	13
Figure 13.	Surface Amplitude: Y Component of Velocity	13
Figure 14.	Surface Amplitude: Z Component of Velocity	14
Figure 15.	Path of Spatial and Time Wave Propagation History	14
Figure 16.	Spatial-Time Wave Propagation History: X Component of Velocity	15
Figure 17.	Spatial-Time Wave Propagation History: Y Component of Velocity	15
Figure 18.	Spatial-Time Wave Propagation History: Z Component of Velocity	15
Figure 19.	Canister Shell Boundary: X Component of Velocity	16
Figure 20.	Canister Shell Boundary: Y Component of Velocity	16
Figure 21.	Canister Shell Boundary: Z Component of Velocity	16
	List of Tables	
Table 1.	Group Velocity of S0 and A0 Modes	6
Table 2.	Material Properties	6

This page is intentionally left blank.

Acronyms

A0 Antisymmetric (wave)

DCSS Dry Canister Storage System

FY Fiscal Year

FEM Finite Element Model
RMS Root Mean Square
S0 Symmetric (wave)

SENSOR DEVELOPMENT FOR LIQUID WATER DETECTION IN DRY STORAGE CASKS: FY 2023 STATUS

1. INTRODUCTION

Modeling efforts were undertaken in fiscal year (FY) 2023 to evaluate the feasibility and capability for sensing of liquid water inside canister-based dry cask storage systems (DCSSs). The focus was on the development of full-scale finite element models (FEMs) of ultrasound propagation through DCSS canister components. For these initial investigations, simulation of the baseplate component was targeted, envisioning water collection at the bottom of a vertically oriented canister. The effects of internal canister components (i.e., fuel basket, fuel assemblies) on ultrasound propagation in the baseplate component were evaluated in these efforts.

The environment inside a DCSS confinement is intended to be inert and free of water to prevent potential corrosion of used fuel cladding or other internal hardware. Spent fuel assemblies are dried, after storage in water pools, to make sure water has been removed from assembly cavities. However, there is some uncertainty about the amount of residual water potentially left behind in a DCSS after drying processes, because water can become trapped in cavities or other small crevices in the surfaces formed by the fuel cladding, fuel assemblies, and other internal hardware components. Considering the complex space- and time-dependent temperature profiles in DCSSs, water may be in a liquid or gas phase depending on its location in the cask and how long the cask has been in storage.

Evacuating most water and oxidizing agents contained within a canister is recommended by NUREG-1536 (NRC 2010), which covers DCSSs. As summarized by Salazar et al. (2020), existing guidance typically relies on achievable vacuum pumping pressures sustained over a hold period as a signal of dryness and water removal. However, time series data about water removal from full-scale commercial drying procedures are lacking (Hanson and Alsaed 2019). A review of drying specifications from several vendors led to the conclusion that if the specifications are followed correctly, the residual moisture in DCSSs should present an insignificant risk of cladding degradation (Knoll and Gilbert 1987). A more recent analysis concluded that much larger quantities of residual water could remain in DCSSs, but the amount would still not be expected to lead to significant corrosion of fuel cladding or other internal components (Jung et al. 2013). Industry drying procedures are mostly prescriptive in nature, and operational issues arising during the process could result in incomplete drying. A summary of operational issues and potential negative effects of residual water is provided by Salazar et al. (2019).

Experimental efforts are ongoing to validate the extent of water removal in a DCSS based on drying procedures used at nuclear power plants through well-designed investigations of drying process efficacy and water retention (Durbin et al. 2021; Pulido et al. 2022a, Pulido et al. 2022b). This has been approached by simulating limited portions of a DCSS internal volume and fuel assemblies. So far, these efforts have focused on the effects of potential water trapping in the dashpot region of control rod guide tubes but are expected to be expanded to include the effects of other internal hardware features and failed fuel rod cladding. A method for detection and measurement of liquid water (Meyer et al. 2022; Meyer et al. 2021), in tandem with the drying information gained through experimental investigations, provides comprehensive bases for understanding the internal conditions of DCSSs and provides technical information to support licensing decisions.

This work proposes sensing of liquid water collecting on the baseplate of a vertically oriented canister via transducers mounted to the external circumference of the baseplate. Externally mounted transducers are desirable because they can be retrofitted to existing DCSSs without requiring physical penetration of the confinement boundary. Techniques such as direct gas sampling introduce risks to inadvertent radiological material releases. The measurement technique described here can facilitate the direct observation of residual water in the field without risk of radiological material release and help establish operational data that can inform operating and licensing decisions for extended storage periods.

This report addresses a technique for water sensing based on the transducer configuration depicted in Figure 1, which shows a model of a nominal baseplate component with a drain sump feature. The input excitation is applied at the position marked 0° on the baseplate circumference and responses are primarily considered to be received at the 0° , 90° , and 180° locations.

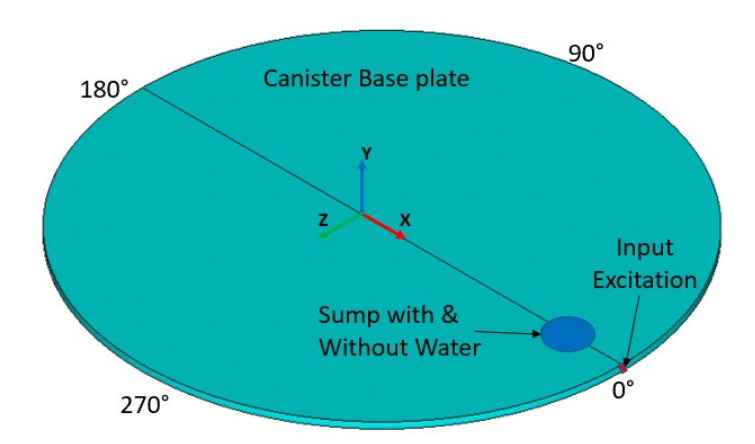


Figure 1. Depiction of a nominal baseplate component with excitation applied at the 0° location on the baseplate circumference.

Previous FEM studies (Meyer et al. 2022) only considered unloaded canister baseplates without fuel assembly or basket weight. The modeling efforts undertaken in FY 2023 included representations of these components to simulate basket and fuel assembly weight loaded onto the canister baseplate.

1.1 Sensing Approach

The sensing technique explored in this effort is based on the propagation of guided ultrasonic Lamb waves within the baseplate component. Lamb wave modes are a particular type of wave mode supported in plate geometry and result from the introduction of low frequency stress waves. At these low frequencies, the ultrasonic signals experience significant interactions with the component boundaries resulting in the formation of modes with propagation characteristics dependent on both the material properties and component dimensions. Dispersion relationships for the group velocity as a function of frequency-thickness for a plate geometry are displayed in Figure 2. This figure shows that many modes can be generated and supported in the structure, including the fundamental modes for antisymmetric (A0) and symmetric (S0) waves and many higher order modes with increasing frequency-thickness. The shaded area to the left of the figure represents the desired region of operation as it minimizes the generation of extraneous higher order modes that complicate signal analysis and interpretation. Figure 3 provides an exaggerated visual depiction of displacement profiles for S0 and A0 modes of vibration produced in the structures under each isolated mode of excitation. It is the displacement component out of the plane of the structure surface that allow these modes to be sensitive to water in contact with the surface of a structure.

In previous efforts, Meyer et al. (2021) applied this sensing technique to a bare-fuel cask system application and were able to demonstrate detection capability to water and a monotonic relationship between water quantity and response to the A0 mode. In this report, the sensing technique is applied to canister-based systems and a detailed examination of the effects of internal hardware on the ultrasonic signals is performed.

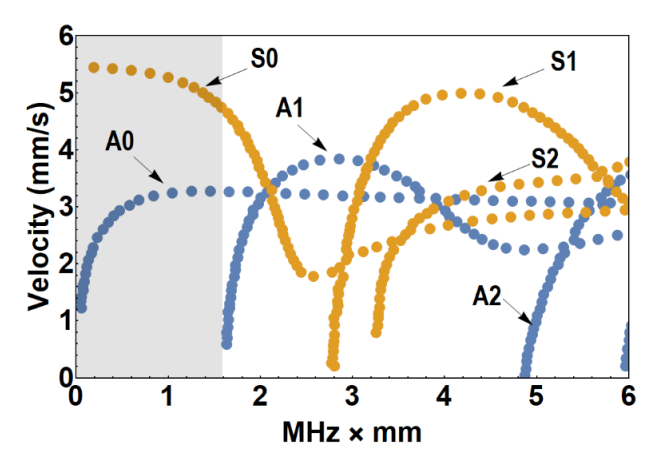


Figure 2. Dispersion curves for group velocities of antisymmetric and symmetric modes. The vertical axis shows the mode group velocity, and the horizontal axis is the frequency-thickness product for a plate structure.

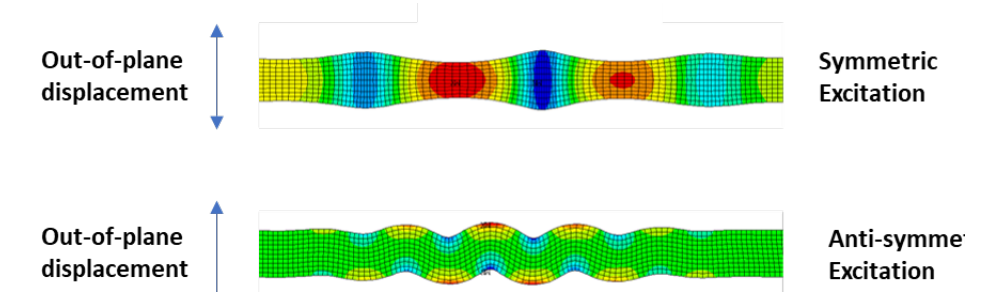


Figure 3. Wave modes in the wall under symmetric and antisymmetric excitation

1.2 Report Contents and Organization

Section 2 summarizes the FEM model incorporated for this effort and includes a description of the modeled geometry and the definitions of material properties. The boundary conditions and load conditions used in the FEM simulations are summarized in Section 3. Results from the simulations performed with truncated representations of internal structures are provided in Section 4. The presentation of results focuses on the effect internal structures have on the components of velocity oscillations introduced by the guided wave excitations. Finally, Section 5 provides some discussion and conclusions, as well as suggestions for future efforts. Appendix A presents results from a simplified model investigating the influence of applied load and local stress on longitudinal wave propagation.

This page is intentionally left blank.

2. FINITE ELEMENT MODEL DESCRIPTION

This section describes the LS-DYNA FEM generated to simulate guided waves in the cask canister baseplate. The intent of this work was to incorporate the basket and fuel assembly geometries to investigate the effect of internal weight on guided wave signals. The details of the model geometry, finite element mesh, material properties, and model assumptions are discussed.

2.1 Geometry

The geometry of the cask canister model is generic and consists of a 2 m diameter, 1 in. thick cask baseplate resting on a rigid plane with truncated representations of the internal basket and surrogate fuel assemblies. The cask outer shell also was truncated to reduce the computational domain. A 6 in. diameter, 0.5 in. deep eccentric drain sump is located 6 in. from the cask outer edge. Half symmetry was used in the model. Regions in which the cask internals cover the drain sump were removed as this section does not carry any weight. Figure 4 presents the geometry of the cask canister model used in the simulations.

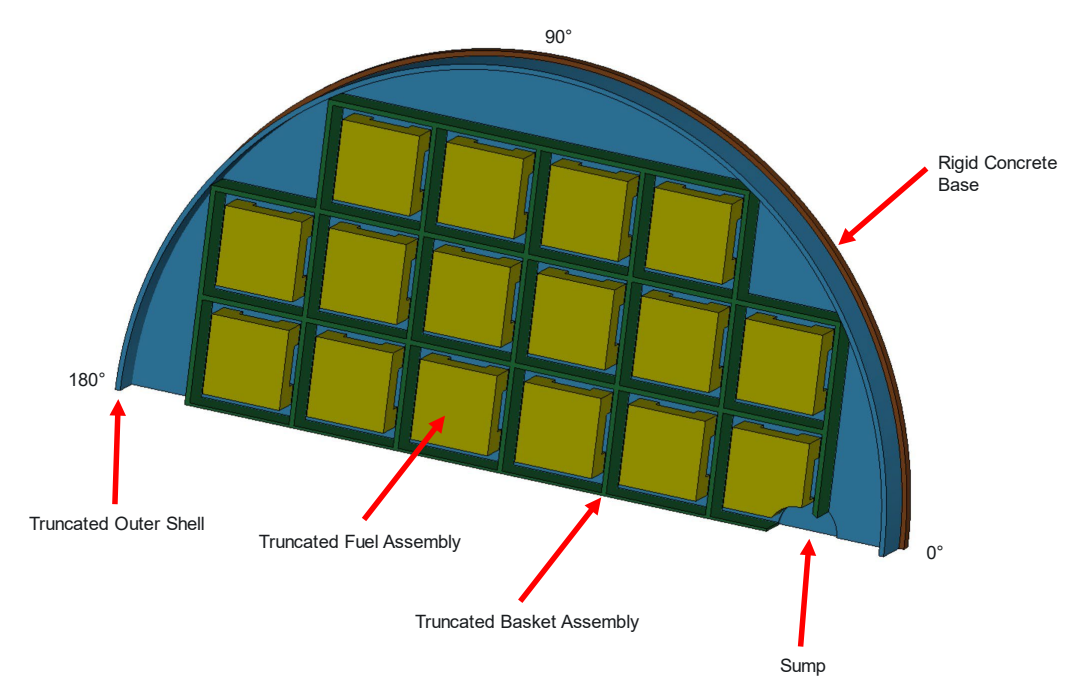


Figure 4. Cask Canister Geometry

The mesh density of the canister baseplate was chosen such that approximately 12–20 elements existed per wavelength of the slowest wave mode. The wavelength of elastic and guided waves is calculated from Equation 1.

$$\lambda = \frac{c}{f} \tag{1}$$

where c is the wave propagation speed and f is the excitation signal frequency. For elastic waves, the wave propagation speed for longitudinal and shear waves are calculated from Equation 2 and Equation 3, respectively.

$$c_l = \sqrt{\frac{K + \frac{4}{3}G}{\rho}} \tag{2}$$

$$c_s = \sqrt{\frac{G}{\rho}} \tag{3}$$

Where K, G, and ρ are the bulk modulus, shear modulus, and density of the material, respectively. For guided waves, the fundamental S0 and A0 wave propagation speeds are derived from dispersion curves at the desired frequency thickness product. The guided wave propagation speeds or group velocity for 36 kHz and 1 in. plate thickness are listed in Table 1.

Table 1. Group Velocity of S0 and A0 Modes

Mode	Group Velocity (m/s)
S0	5000
A0	3200

2.2 Material Properties

The material properties used in the models were linear elastic, with the concrete base having a rigid material model. The material constants in the rigid material model serve only to develop the contact interface properties (e.g., contact stiffness). The material properties are listed in Table 2.

Table 2. Material Properties

	Elastic Modulus (GPa)	Density (kg/m ³)	Poisson Ratio
Cask Canister Disk	200	7,800	0.29
Basket	200	689,000*	0.29
Fuel Assemblies	200	309,000*	0.29
Concrete Base	200	7,800	0.29
*D : Cd 1 1 1 1	C 1 11: 1		0.1

^{*} Density of the basket and fuel assemblies were adjusted to be representative of the internal weight.

3. LOADS AND BOUNDARY CONDITIONS

A major difficulty in simulating guided waves with weight/gravity loads is in achieving a steady state preload to a resolution where guided waves can be detected. Elimination of the inertial effect experienced by the cask baseplate and internal components comes at a high computational cost given the mesh density required for the model. To reduce the computation time, the model was solved in three separate sequential analysis phases: 1) an implicit preload analysis, 2) a damped transient analysis, and 3) the guided wave transient analysis. Separation of these phases of the solution facilitates solving for the steady-state preload condition only once.

Frictionless contact was defined to represent all interfaces in the model (canister baseplate – rigid concrete, and canister baseplate – internal components). This was chosen to eliminate friction as a variable in studying the influence of internal component weight on guided wave signals. The truncated outer shell was prescribed with absorbing boundary conditions to eliminate non-physical reflections from re-entering the cask baseplate domain.

3.1 Implicit Pre-Load Analysis

The implicit preload analysis serves to solve for the steady-state solution of the cask baseplate and internal components under gravity loading with an implicit solver. Minimum boundary conditions are applied to all components of the model, with the concrete base constrained in all directions. From preliminary analyses, it was determined that applying an additional symmetry constraint on the basket (normal to the center line of the disk) further reduces the inertial effect of the basket during later phases. Although this is an over-constraint, only the application of the load in the vertical direction is of interest. The solution of the implicit pre-load analysis is written in a nodal displacement file, which is read back into the model in later phases.

3.2 Damped Transient Analysis

The application of the pre-load from the implicit solution is then established for further transient analyses via a preliminary pseudo-transient analysis in which the nodal displacements from the implicit pre-load solution are linearly ramped over a user specified time interval. It was found that residual kinetic energy still existed in the system after the model was prescribed the pre-load displacements. Hence, a damped transient analysis is conducted to remove the residual energy. To determine appropriate damping, an undamped transient analysis was conducted to determine the frequency content in the model after the preload was applied. The rigid body displacements and corresponding fast Fourier transform can be seen in Figure 5.

Mass proportional damping was applied to each part to remove the residual energy in the system. Favorable damping is some value approaching the critical damping constant (D_C), defined by Equation 4.

$$D_c = 2\omega \tag{4}$$

where ω is the frequency of interest. The frequencies targeted for mass proportional damping were 930 Hz, 133 Hz, and 399 Hz for the canister baseplate, basket, and fuel assemblies, respectively. The percentage of critical damping applied to each part and the resulting rigid body displacement during the damped transient analysis are shown in Figure 6 and Figure 7, respectively. In Figure 7 (Bottom), the displacements were shifted for viewing purposes. The reason for time-varying damping was to accelerate the resolution of any resultant rigid body displacements early in the simulation. As can be seen, the solution reaches a displacement steady state resolution within an order of magnitude of 1E-11 m. Damping is removed after the damped transient analysis.

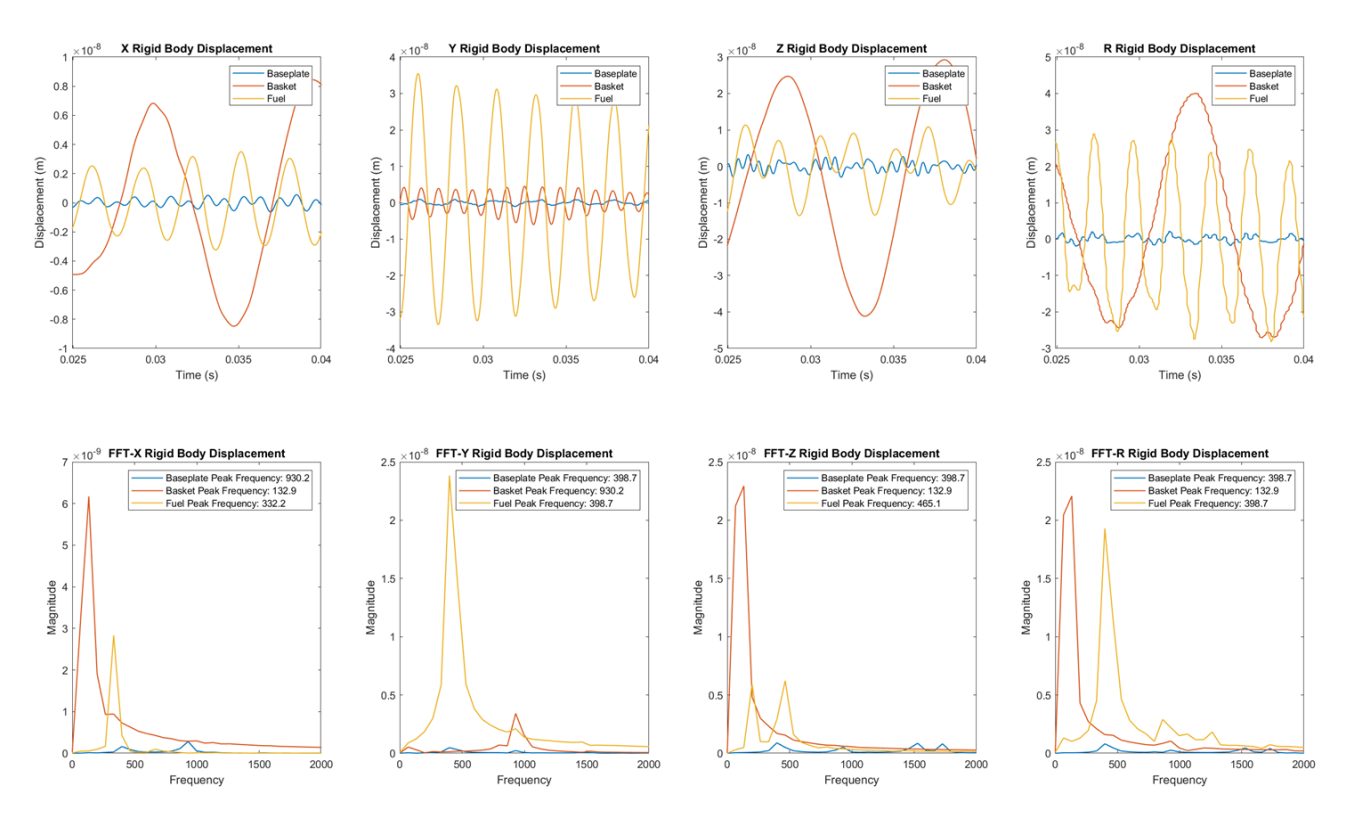


Figure 5. Undamped Transient Analysis Post-Preload

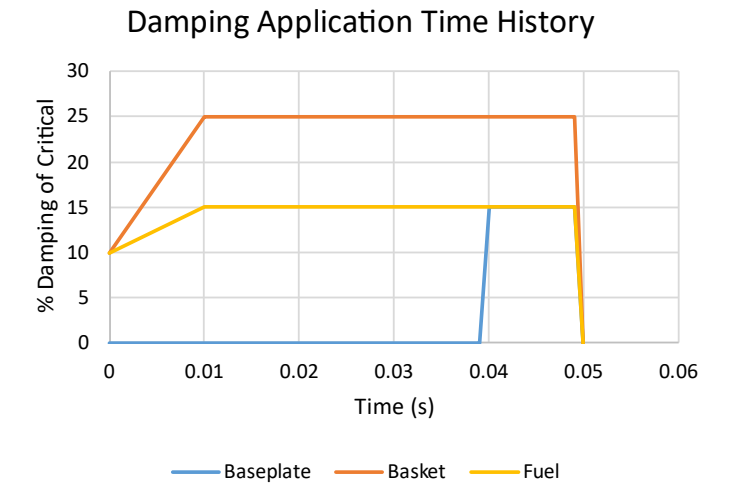


Figure 6. Damping Application Time History

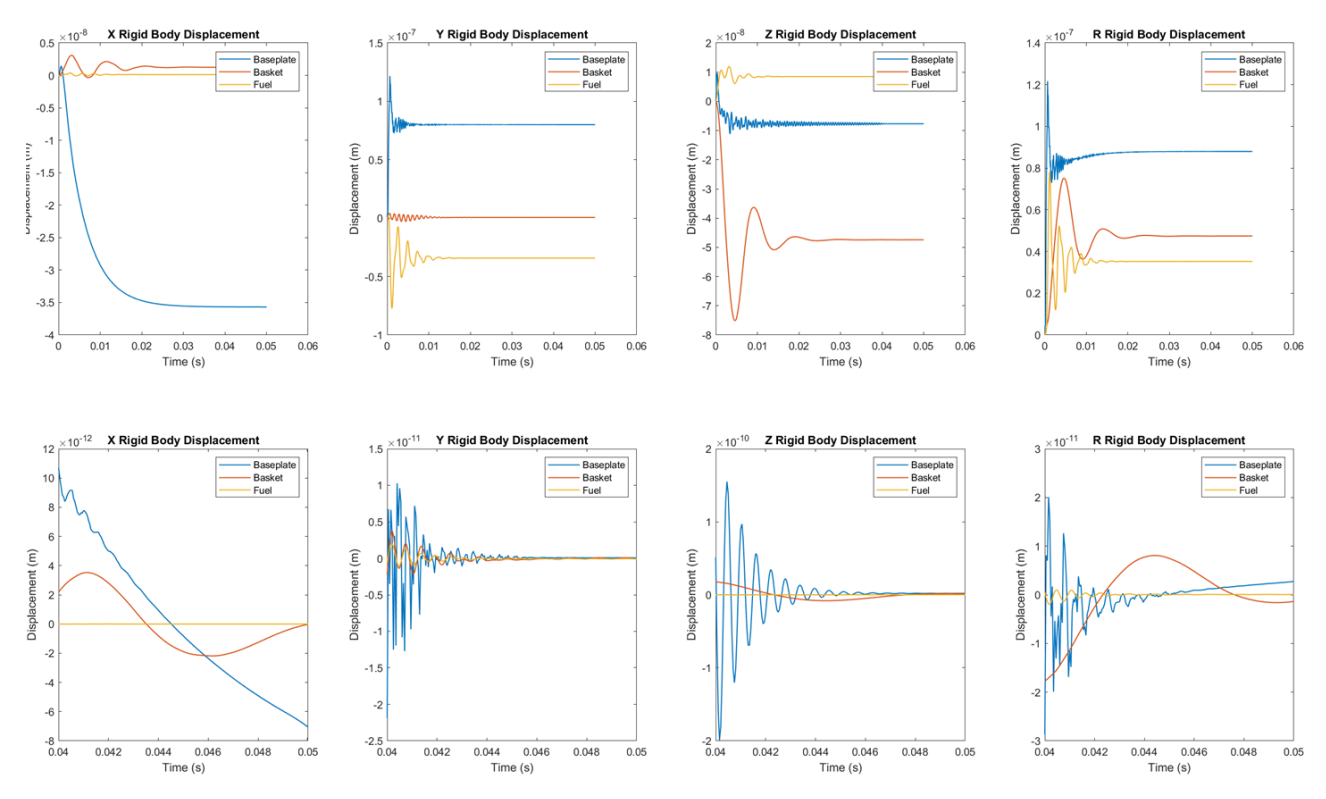


Figure 7. System Rigid Body Displacement

3.3 Guided Wave Transient Analysis

The guided wave transient analysis is conducted by application of a 36 kHz, 1N, five-cycle Hann windowed sinusoidal pulse over nodes in a 1 in² area on the edge of the canister disk at the 0° location. The S0 mode was excited by applying the excitation normal to the edge of the baseplate. Excitation of the A0 mode will be investigated in future studies. The excitation time history can be seen in Figure 8. All boundary conditions and contact conditions remain unchanged from previous analyses.

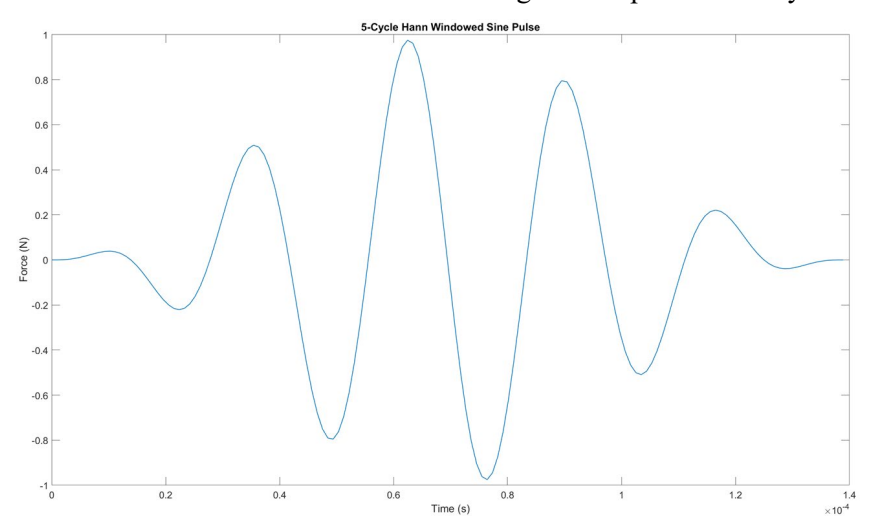


Figure 8. Input Excitation Signal

This page is intentionally left blank.

4. RESULTS

This section presents results comparing the baseline model and the loaded canister model. The baseline model contains no internal components but includes gravity and the rigid concrete base. Comparison between the baseline model and the loaded canister model can provide valuable insight to the differences that can be expected in the guided wave signals, as well as help inform the effect of internal weight on the physics of the problem. Nodal velocities were the metric chosen to measure signal amplitude, and a low pass filter with a cut-off frequency of 36 kHz was applied to all time histories reported.

Figure 9 through Figure 11 illustrate the root mean square (RMS) nodal velocity of the 1 in.² group of nodes at the 0°, 90°, and 180° locations of the baseplate in each cartesian direction. The RMS of the resulting signal was calculated and listed in the legend of each figure. It is observed that the RMS of the received signals are reduced at the 90° location and increased in 180° location when the weight of the cask internals is included. This phenomenon is readily seen in the out-of-plane (Y) component in the signal (Figure 10), which demonstrates significant amplification of the signal in the 180° location. This suggests less of the guided wave energy is traveling along the perimeter of the canister, which could result from either 1) redirection of the wave energy or 2) energy loss out of the domain. Further, increased levels of noise are visible in the out-of-plane component of the signal at the 0° location, indicating returning vibrations after excitation of the wave.

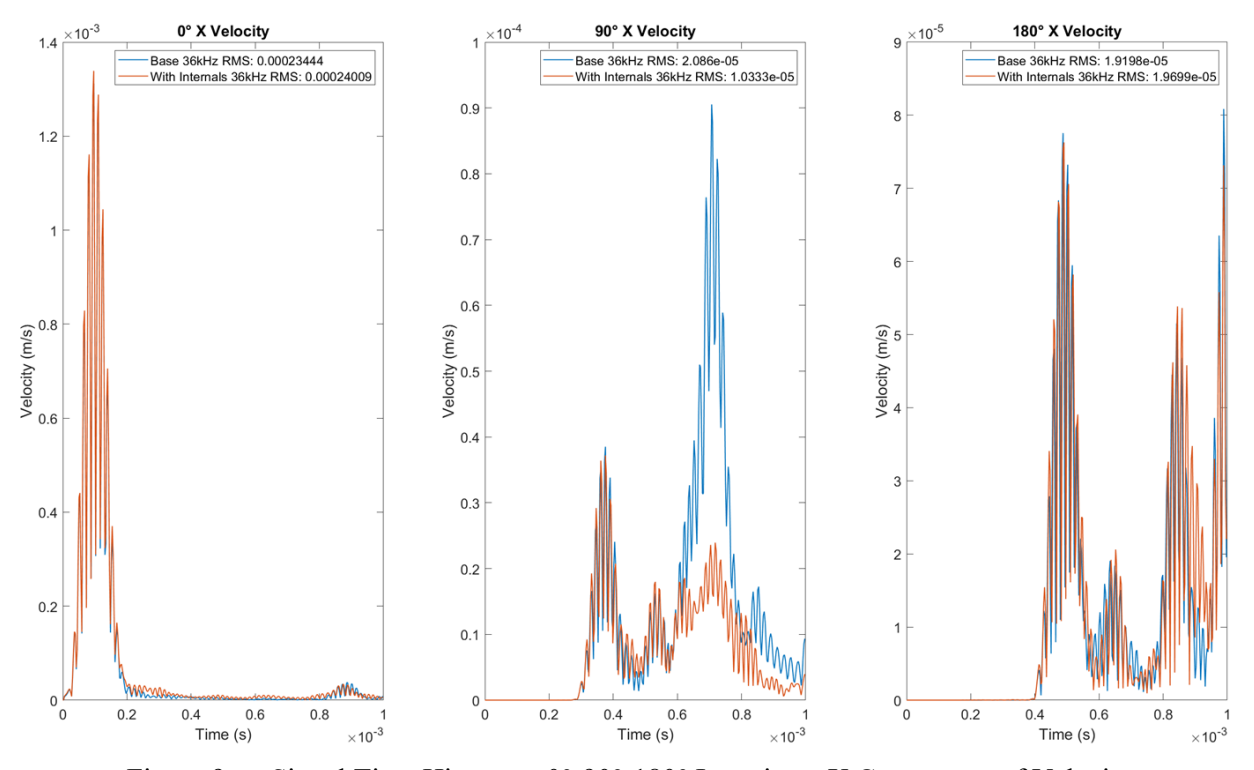


Figure 9. Signal Time History at 0°-90°-180° Locations: X Component of Velocity

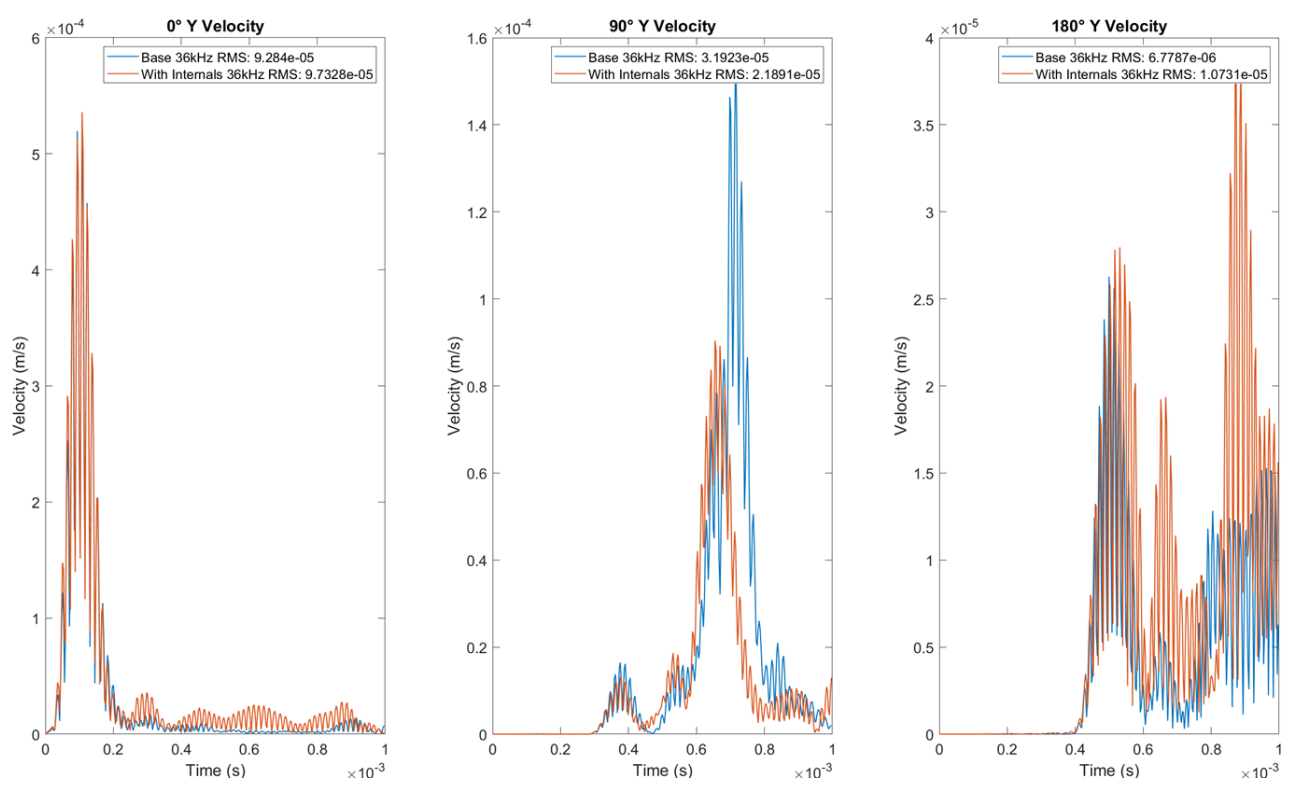


Figure 10. Signal Time History at 0°-90°-180° Locations: Y Component of Velocity

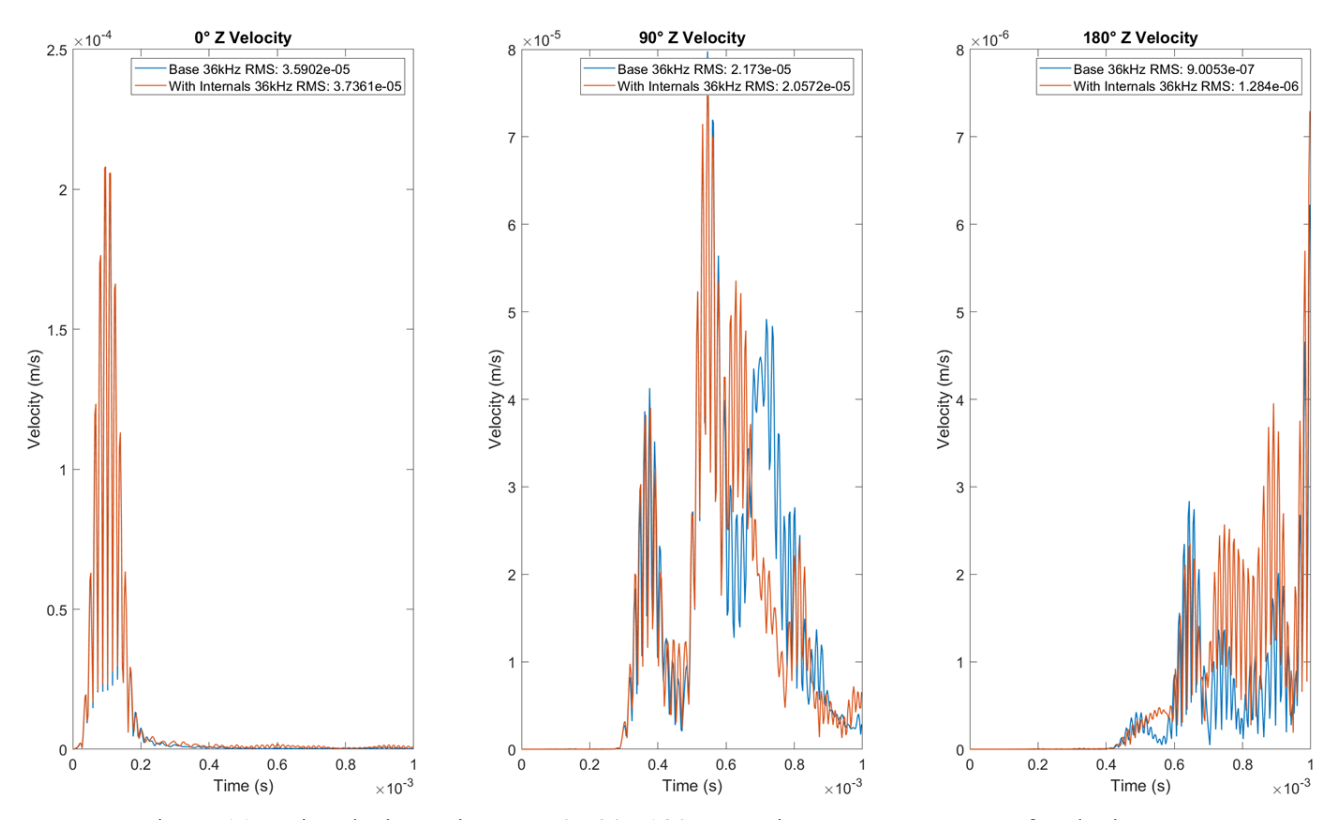


Figure 11. Signal Time History at 0°-90°-180° Locations: Z Component of Velocity

To compare the global wave propagation characteristics with internal weight, Figure 12 through Figure 14 display two-dimensional views of the positive-only nodal velocities on the top surface of the baseplate from time 0 ms to 1 ms. The color scale was equivalent between both models and truncated to better view the low amplitude waves propagating in the plate. The figures for the model with cask internals contain a transparent overlay of the internal component footprint.

It is observed in Figure 13 (Right) that large scattering of the out-of-plane component of the wave is present as the wave encounters the loaded sections of the baseplate. The signal amplitude is amplified and redirected locally at the boundaries of the internal components. This contrasts with the baseline case (Figure 13 Left) where the out-of-plane component propagates uniformly through the plate. The loaded sections of the baseplate present local thickness variations and an out-of-plane boundary condition, resisting the out-of-plane component from propagating underneath the weight. Thus, the loaded sections of the baseplate disrupt the free propagation characteristics of the wave, resulting in local wavefront distortions, mode conversion, and scattering. The observation of localized maxima of the out-of-plane component could be attributed to the interactions/superposition of the scattered out of plane components of the wave. Similar scattering behavior was observed in plates with random thickness variation in Ferguson (2022).

As a result, localized peaks in the out-of-plane velocity from scattering are found to be propagating along the center of the baseplate, and less energy is propagating along the perimeter. Fluctuations observed in the in-plane velocity components (Figure 12 and Figure 14) could be the result of momentum transfer/balance with the out-of-plane scattering. A similar phenomenon is observed in a simplified case study in Appendix A (Figure A.5 and Figure A.6) where the local maximum out-of-plane amplitude corresponds to a local minimum in the in-plane signal amplitude.

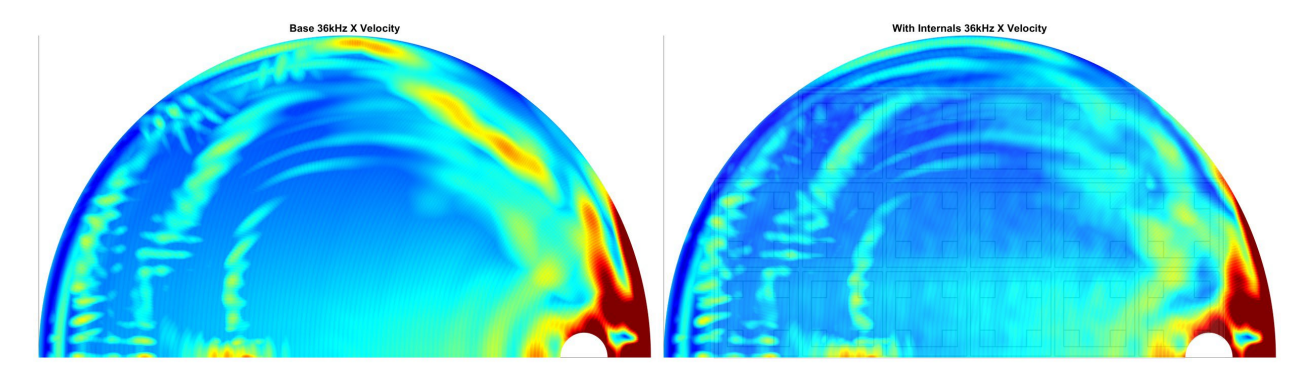


Figure 12. Surface Amplitude: X Component of Velocity

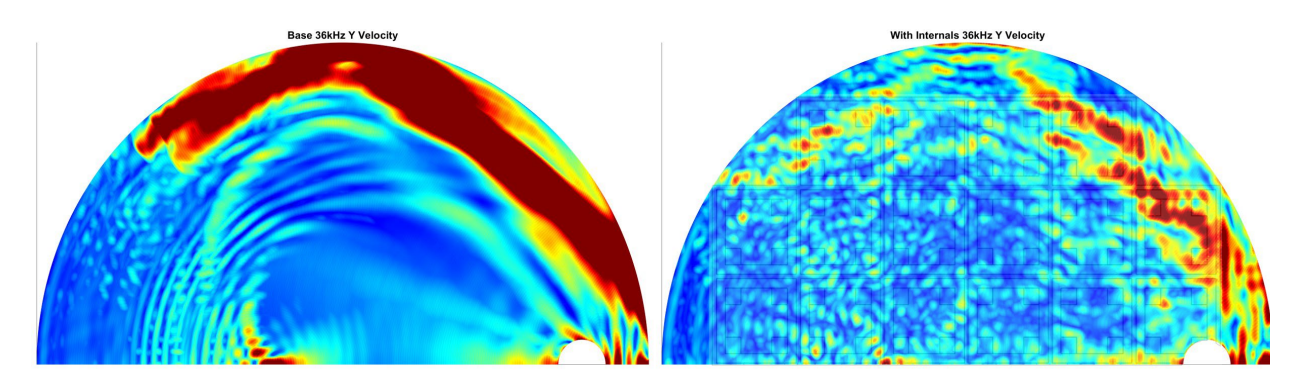


Figure 13. Surface Amplitude: Y Component of Velocity

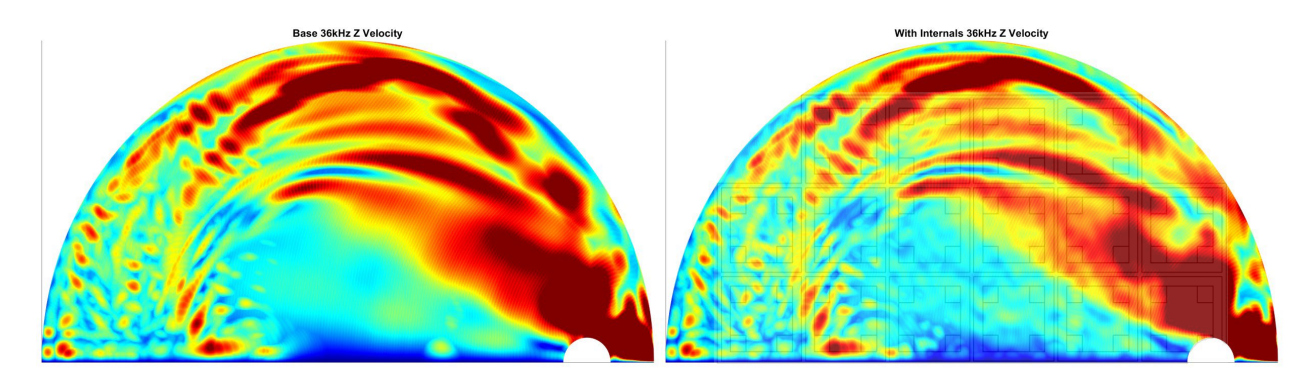


Figure 14. Surface Amplitude: Z Component of Velocity

Figure 16 through Figure 18 illustrate the spatial and time wave propagation history along the path illustrated in Figure 15 for both the baseline and loaded canister model. This path represents wave propagation underneath the basket sections and the fuel assembly legs in the loaded canister model. The edges of the fuel assembly legs are superimposed onto the figures using vertical magenta-colored lines, and the edges of the basket sections are represented as blue lines. It is readily observed in Figure 17, that interactions with the basket and fuel assembly legs result in local wavefront distortions and reflections. Reflections are characterized by equal and opposite wavefronts propagating in the opposite direction. Reflections are most notably observed in the in-plane (X) and out-of-plane (Y) components (Figure 16 and Figure 17). Therefore, the increased noise observed in the signal response of Figure 10 can be attributed to reflections of the waves from interaction with the canister internals (see also Figure A.9). Further, these reflections could include contributions of secondary waves produced from re-excitation of the internal components (see Figure A.10). The presence of mode conversion is also captured, characterized by the two distinct wavefronts having varying slope/velocity. This mode conversion could be the result of both interaction with the empty sump as well as wavefront distortion from the loaded sections of the canister baseplate.

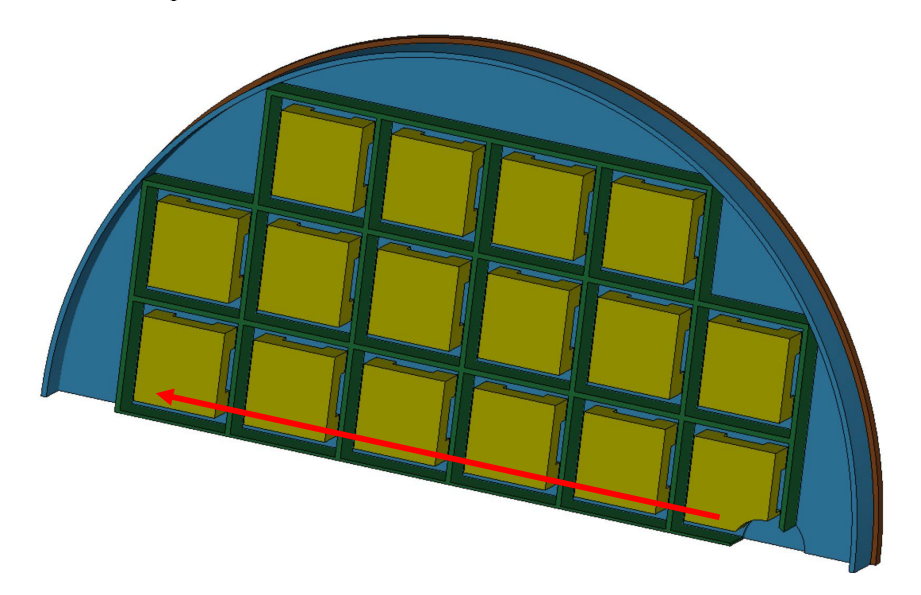


Figure 15. Path of Spatial and Time Wave Propagation History

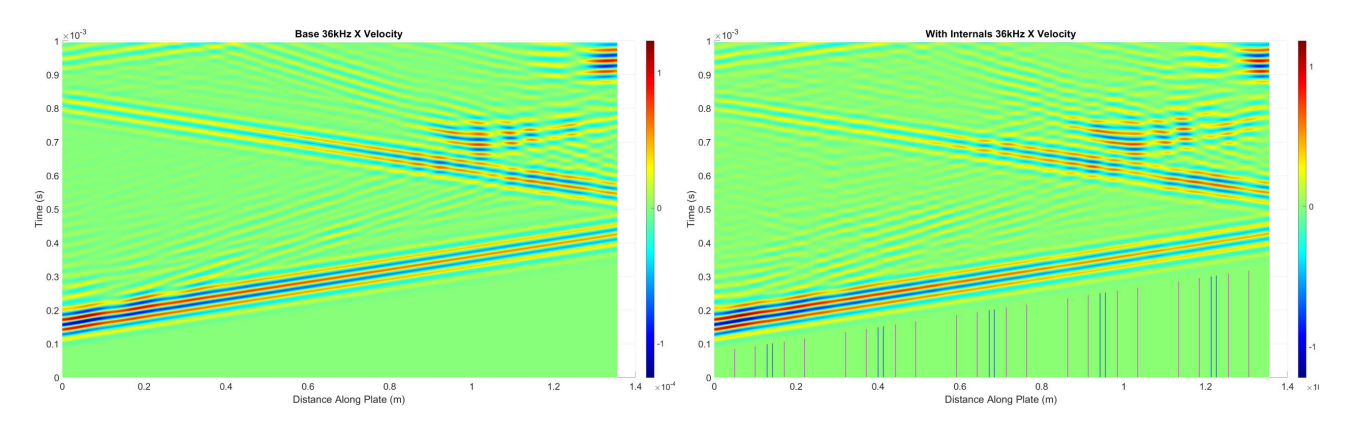


Figure 16. Spatial-Time Wave Propagation History: X Component of Velocity

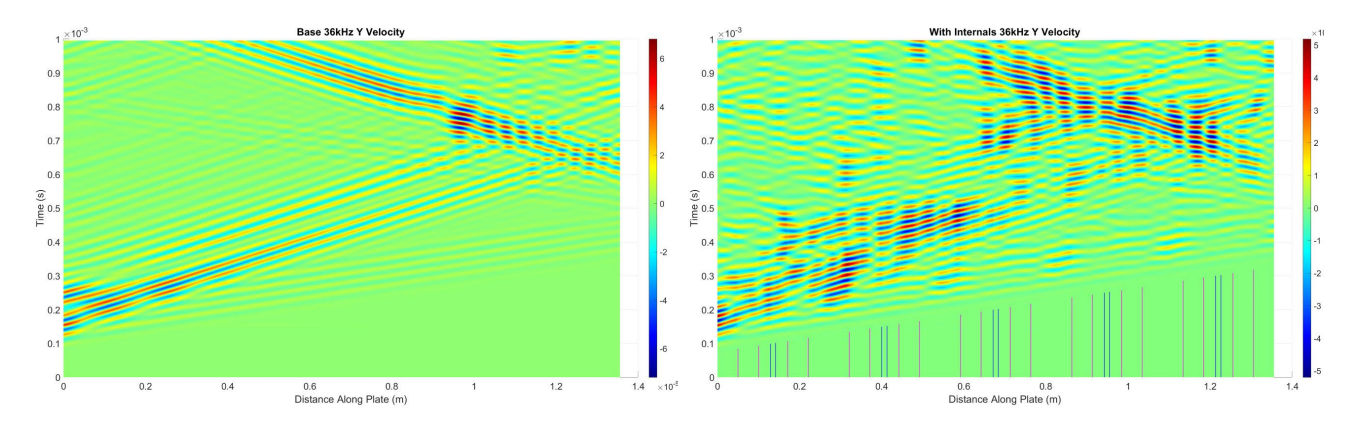


Figure 17. Spatial-Time Wave Propagation History: Y Component of Velocity

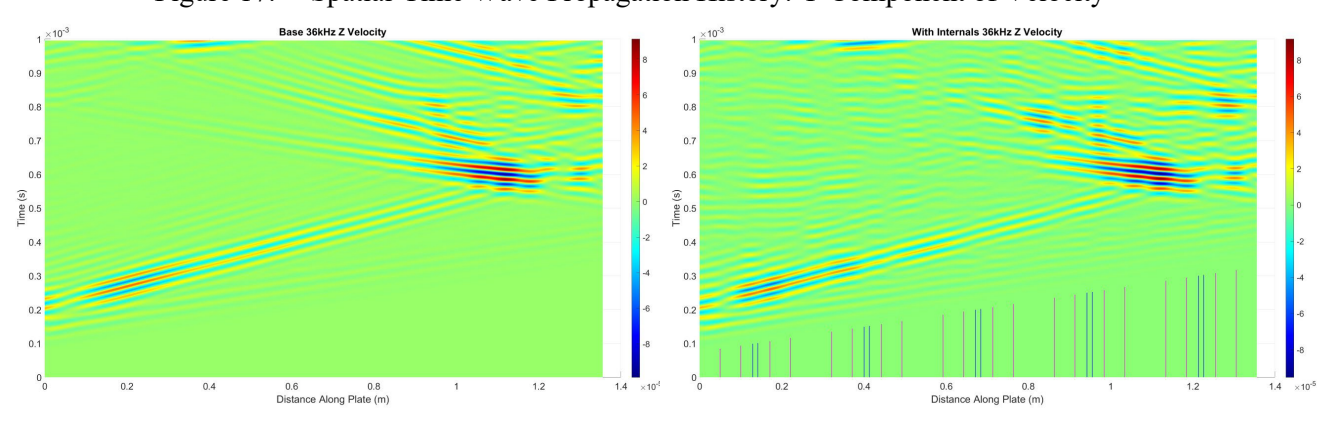


Figure 18. Spatial-Time Wave Propagation History: Z Component of Velocity

Evidence of wave reflection/refraction suggests the possibility of increased energy loss to the canister shell. This can be seen in Figure 19 through Figure 21, which illustrate a three-dimensional representation of the positive-only nodal velocity amplitude at the boundary of the outer shell from 0–1 ms. Increased amplitudes are found to exist at the shell boundary of the loaded canister model, indicating higher energy losses in the system. After initial excitation, the wave encounters the outside edge of the basket, resulting in reflections back toward the canister boundary. This phenomenon contributes to the observation of decreased wave energy travelling along the circumference of the disk in the loaded canister model.

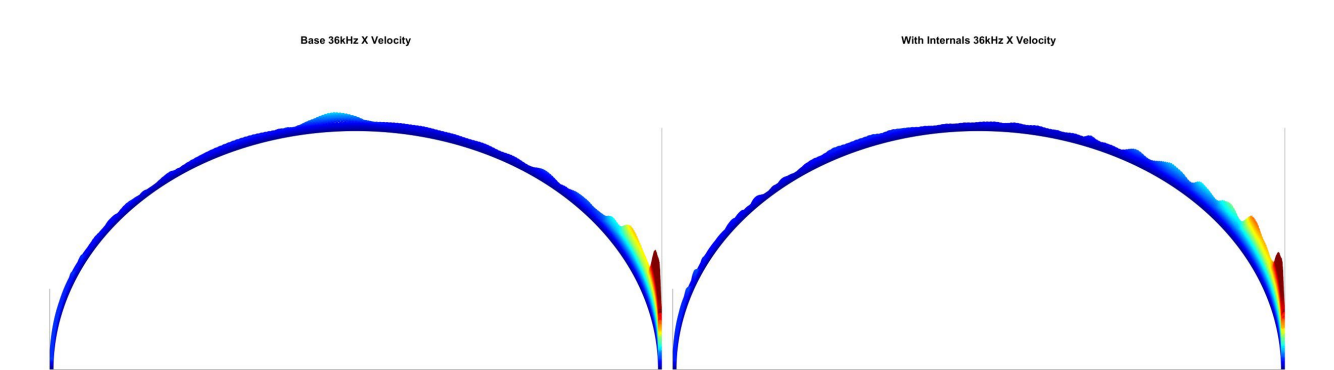


Figure 19. Canister Shell Boundary: X Component of Velocity

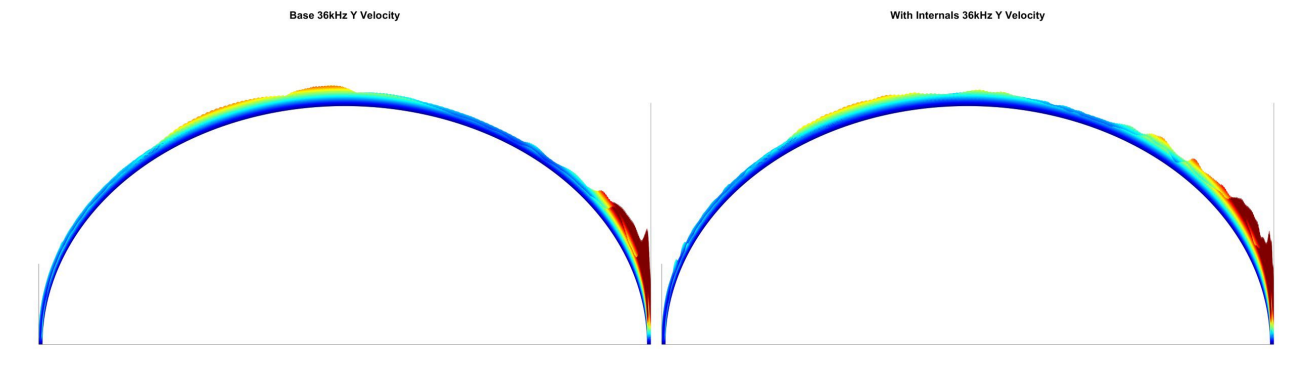


Figure 20. Canister Shell Boundary: Y Component of Velocity

Base 36kHz Z Velocity

With Internals 36kHz Z Velocity

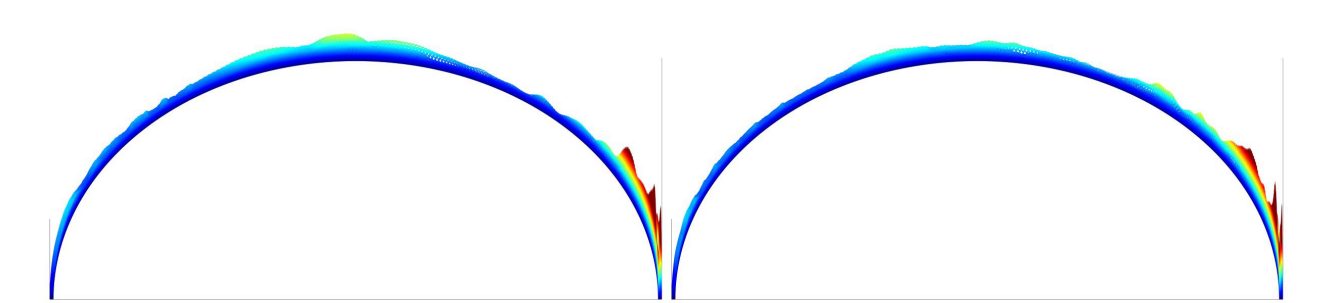


Figure 21. Canister Shell Boundary: Z Component of Velocity

5. SUMMARY, CONCLUSIONS, AND FUTURE EFFORTS

The inclusion of basket and fuel assembly weight on the cask canister baseplate generate local surface non-uniformity and a restrictive out-of-plane boundary condition at the locations where the canister baseplate is loaded. These deviations from the ideal, unloaded, uniform surface condition disrupt the free propagation characteristics of guided waves, resulting in local wavefront distortions. As a result, scattering behavior and mode conversion occurs, causing wave energy to propagate in different directions within the plate. This resulted in varying RMS levels in the received signals at the 0°, 90°, and 180° locations on the plate. The reflections from scattering also increased the noise level in the signals and resulted in increased energy loss to the canister shell.

Note that only the S0 mode at a single frequency (36 kHz) without the presence of water in the sump was investigated in this work. However, the increased noise and varying RMS levels from the forementioned phenomenon may affect the quality of signals in water detection scenarios. Future studies shall consider 1) the inclusion of water in the canister sump, 2) alternate modes of excitation, and 3) varying frequencies of excitation. Further, the effect of friction at the contact interfaces could be explored. Efforts to validate the numerical studies and hypotheses with experimental results are also recommended.

This page is intentionally left blank.

6. REFERENCES

ANSYS 2020 R1, ANSYS Inc., Southpointe, 2600 ANSYS Drive, Canonsburg, Pennsylvania.

Durbin SG, ER Lindgren, RJ M. Pulido, A Salazar III, RE Fasano. 2021. Update on the Simulation of Commercial Drying of Spent Nuclear Fuel. Department of Energy, Spent Fuel and Waste Science and Technology Sandia National Laboratories M2SF-21SN010203033; SAND2021-11828 R, Albuquerque, Mexico..

Hanson BD and HA Alsaed. 2019. Gap Analysis to Support Extended Storage and Transportation of Spent Nuclear Fuel: Five-Year Delta. Department of Energy Office of Spent Fuel Waste Science and Technology SFWD-SFWST-2017-000005, Rev. 1; PNNL-28711, Washington, D.C.

Jose K, N Ferguson, and ABhaskar, A. Branched flows of flexural waves in non-uniform elastic plates. Commun Phys 5, 152 (2022). https://doi.org/10.1038/s42005-022-00917-z

Jung H, P Shukla, T Ahn, L Tipton, K Das, X He, and D Basu. 2013. Extended Storage and Transportation: Evaluation of Drying Adequacy. Center for Nuclear Waste Regulatory Analyses ADAMS Accession No. ML13169A039, San Antonio, Texas. https://www.nrc.gov/docs/ML1316/ML13169A039.pdf.

Knoll RW and ER Gilbert. 1987. Evaluation of Cover Gas Impurities and Their Effects on the Dry Storage of LWR Spent Fuel. Pacific Northwest Laboratory PNL-6365, Richland, Washington. https://www.osti.gov/servlets/purl/5599035.

Meyer LS-DYNA R12, Livermore Software Technology, 7374 Las Positas Road Livermore, California 94551

Meyer RM, NK Karri, CT Christiansen, and MS Good. 2021. Sensor Development for Liquid Water Detection in Dry Storage Casks: FY 2021 Status. Pacific Northwest Laboratory M3SF-21PN0102030211; PNNL-31786, Pacific Northwest National Laboratory, Richland, Washington.

Meyer RM, NK Karri, C Zhang. 2022. Sensor Development for Liquid Water Detection in Dry Storage Casks: FY 2022 Status. Pacific Northwest Laboratory M3SF-22PN010203028, PNNL-33303, Pacific Northwest National Laboratory, Richland, Washington.

NRC. 2010. Standard Review Plan for Spent Fuel Dry Storage Systems at a General License Facility: Final Report. Department of Energy Office of Spent Fuel Waste Science and Technology NUREG-1536, Rev. 1, Washington, D.C. https://www.nrc.gov/docs/ML1010/ML101040620.pdf.

Pulido RJM, SG Durbin, RW Williams, B Baigas, GT Vice, GJ Koenig, RE Fasano, and A Salazar III. 2022. Update on the Investigation of Commercial Drying Cycles Using the Advanced Drying Cycle Simulator. Department of Energy, Spent Fuel and Waste Science and Technology Sandia National Laboratories M2SF-22SN010203033; SAND2022-12978 R, Albuquerque, New Mexico.

Pulido RJM, A Taconi, A Salazar III, RE Fasano, RW Williams, B Baigas, and SG Durbin. 2022. Response of a Pressurized Water Reactor Dashpot Region to Commercial Drying Cycles. Department of Energy, Spent Fuel and Waste Science and Technology Sandia National Laboratories M2SF-22SN010203032; SAND2022-3813 R, Albuquerque, New Mexico.

Salazar A, R. JM Pulido, ER Lindgren, and SG Durbin. 2019. Advanced Concepts for Dry Storage Cask Thermal-Hydraulic Testing. Sandia National Laboratories SAND2019 11281R, Albuquerque, New Mexico. https://www.osti.gov/servlets/purl/1569153.

Salazar A, ER Lindgren, RE Fasano, RJM Pulido, and SG Durbin. 2020. Development of Mockups and Instrumentation for Spent Fuel Drying Test. Department of Energy, Spent Fuel and Waste Science and Technology Sandia National Laboratories M2SF-20SN010203033, SAND2020-5431 R, Albuquerque, New Mexico. https://www.osti.gov/biblio/1631218/.

This page is intentionally left blank.

APPENDIX A - SIMPLIFIED MODEL CASE STUDY

A simplified finite element model was developed to better understand the effect of weight and surface uniformity on the propagation characteristics of guided waves. The simplified model consists of a 1 in. thick rectangular plate resting on a rigid base with a symmetric boundary condition along the centerline. Non-reflecting boundary conditions were prescribed on the exterior edges of the domain, excluding the excitation edge. A pressure analogous to the pressure applied by the basket was applied at the midway point of the plate length and acting over half of the plate width. The width of the pressure area was equivalent to the basket thickness used in the full-scale model. A figure of the simplified model with applied pressure is shown in Figure A.1.

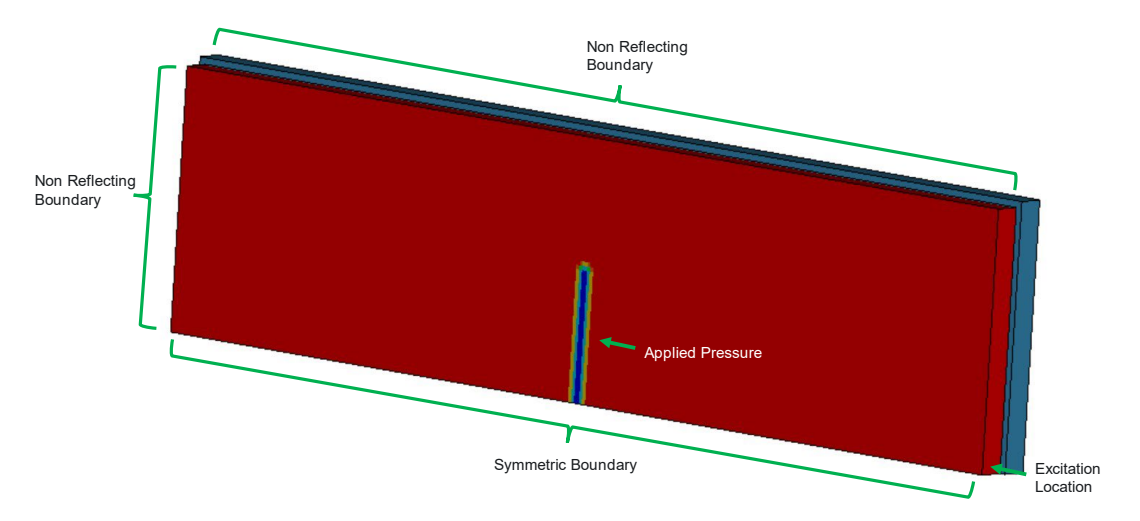


Figure A.1. Simplified Model Geometry

The model loading history was applied equivalently to the full-scale model, which included an implicit preload analysis, damped transient analysis, and the guided wave transient analysis. Further, the material properties, contact conditions, and guided wave excitation method were equivalent between the simplified model and full-scale model. Results from a baseline case without pressure and a loaded case with pressure were compared.

Figure A.3 through Figure A.4 display the component-wise RMS nodal velocity of the surface node at locations specified by Figure A.2. The in-plane (Z) component is omitted because of the symmetry constraint. It is observed that increased levels of noise are present in the model with pressure at the center and end locations. Further, small amplitude vibrations appear at the center and end locations prior to the arrival of the wavefront, whose origin is not well understood. It is believed that the initial excitation at the source introduces an inertial effect at the location of the applied pressure, introducing secondary waves propagating from the center and end locations of the disk due to reactive forces. The signal energy at the "Source" and "End" location is consistent with the full-scale model, with RMS levels greater in the model with pressure due to increased vibratory response.

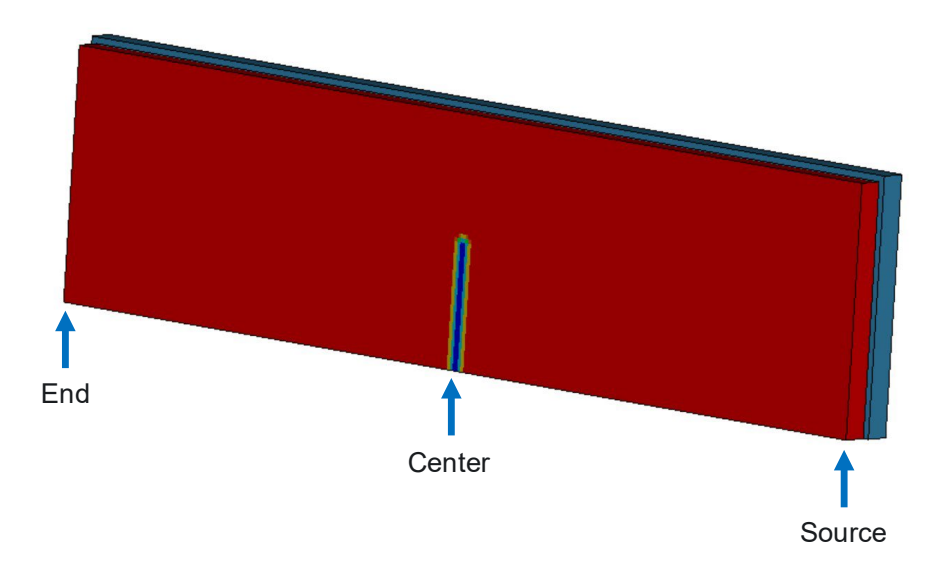


Figure A.2. Simplified Model Signal Response Locations

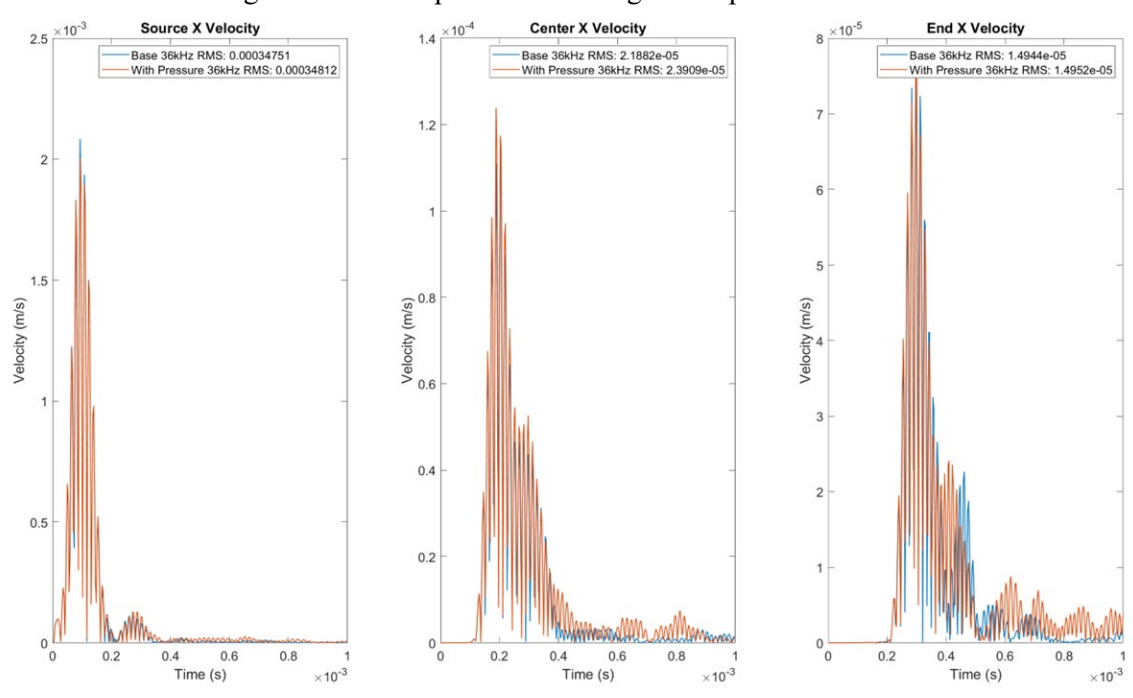


Figure A.3. Signal Time History at Source-Center-End Locations: X Component of Velocity

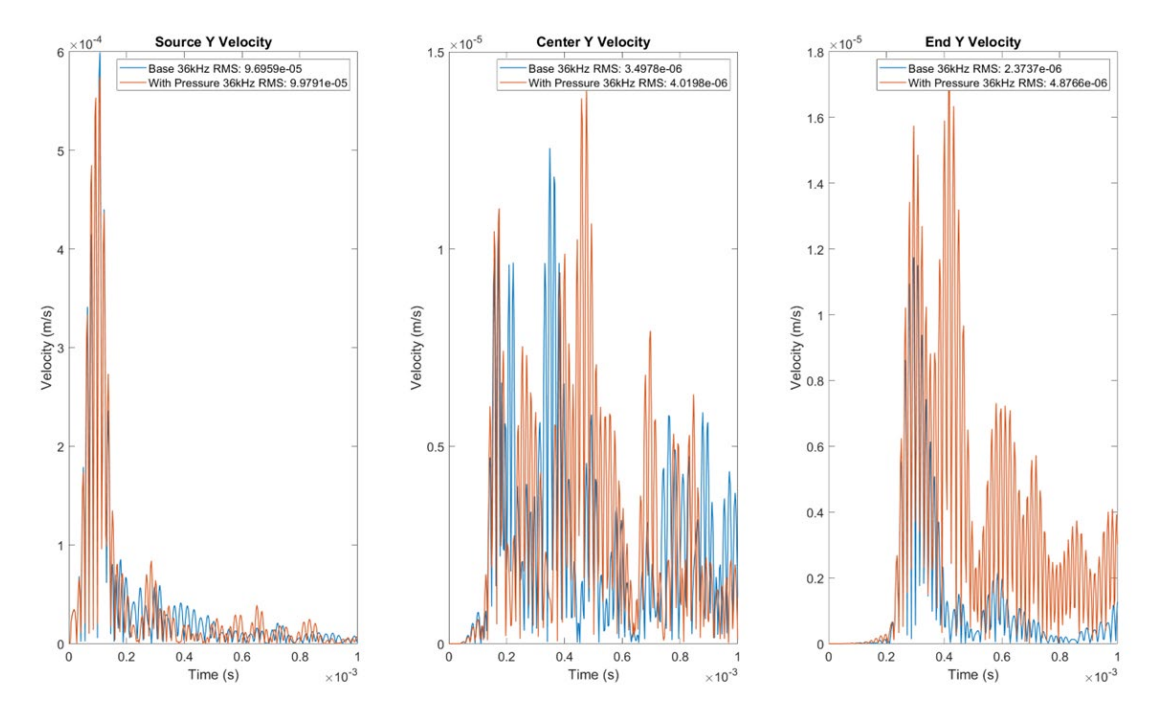


Figure A.4. Signal Time History at Source-Center-End Locations: Y Component of Velocity

To better investigate the global behavior of the wave propagation, a two-dimensional view of the positive-only nodal velocities on the top surface of the plate were plotted from 0 to 0.5 ms (Figure A.5 through Figure A.7). As expected, the out-of-plane (Y) component of velocity is restricted at the center of the plate where the pressure is applied (Figure A.6 Right). Local maximums of out-of-plane velocity occur at the boundaries of the applied pressure. These local maximums and minimums in out-of-plane velocity correspond to local minimums and maximums in the in-plane (X) component of velocity (Figure A.5), suggesting potential momentum balance/transfer due to the restrictive out-of-plane boundary condition supplied by the applied pressure.

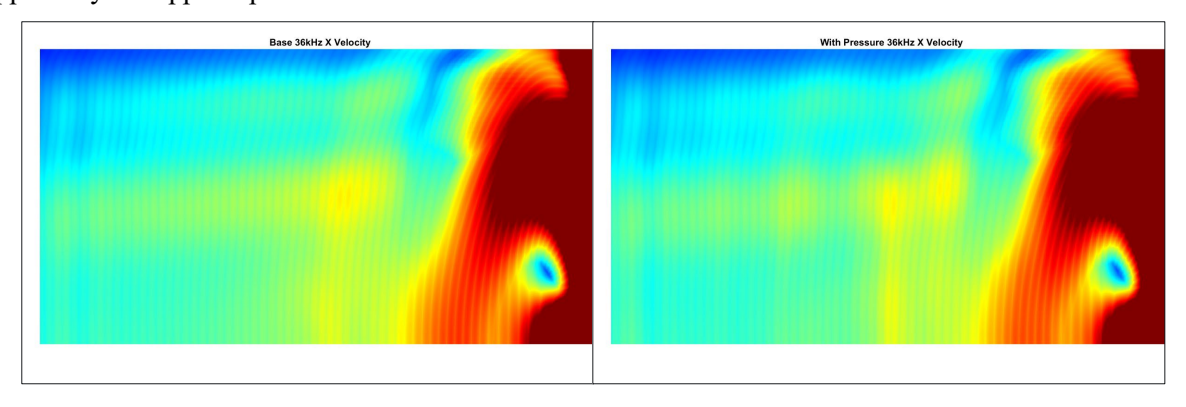


Figure A.5. Surface Amplitude: X Component of Velocity

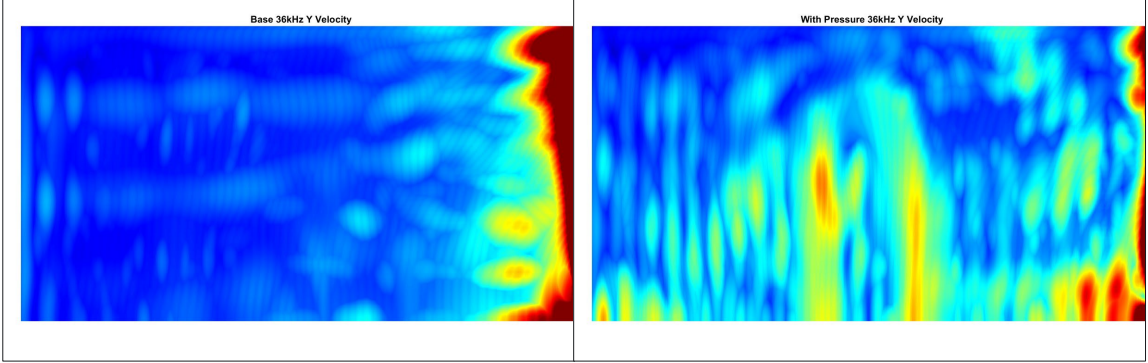


Figure A.6. Surface Amplitude: Y Component of Velocity

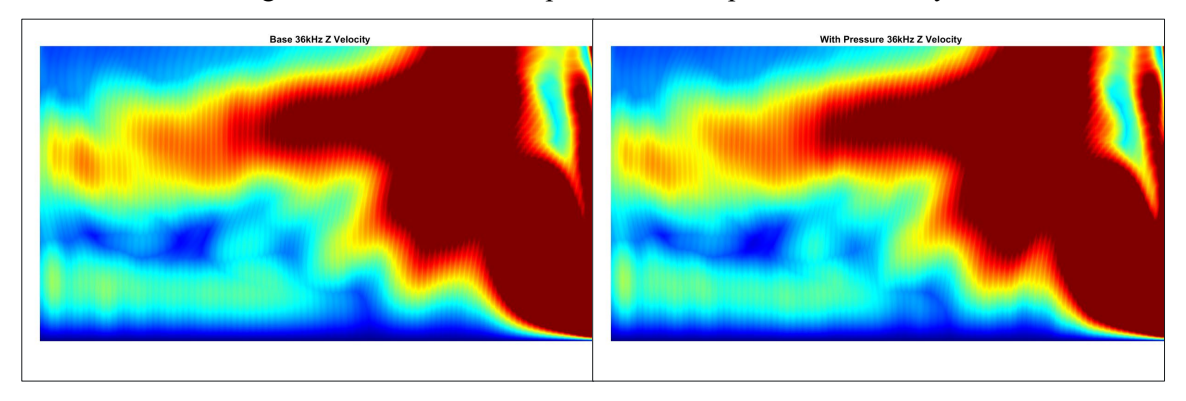


Figure A.7. Surface Amplitude: Z Component of Velocity

Figure A.8 and Figure A.9 illustrate the spatial and time wave propagation history along the centerline of the top surface of the plate for both the baseline and applied pressure model. Both models share an equivalent color scale. Wavefront distortion, reflections, and mode conversion is observed as the wave passes through the applied pressure region (Figure A.9). Additional reflections are captured at the source prior to when the wavefront reaches the applied pressure. Figure A.10 captures excited vibrations at the location of applied pressure prior arrival of the wavefront. This could be due to global excitation of the applied pressure region due to application of the guided wave, introducing additional waves propagating away from the pressure region.

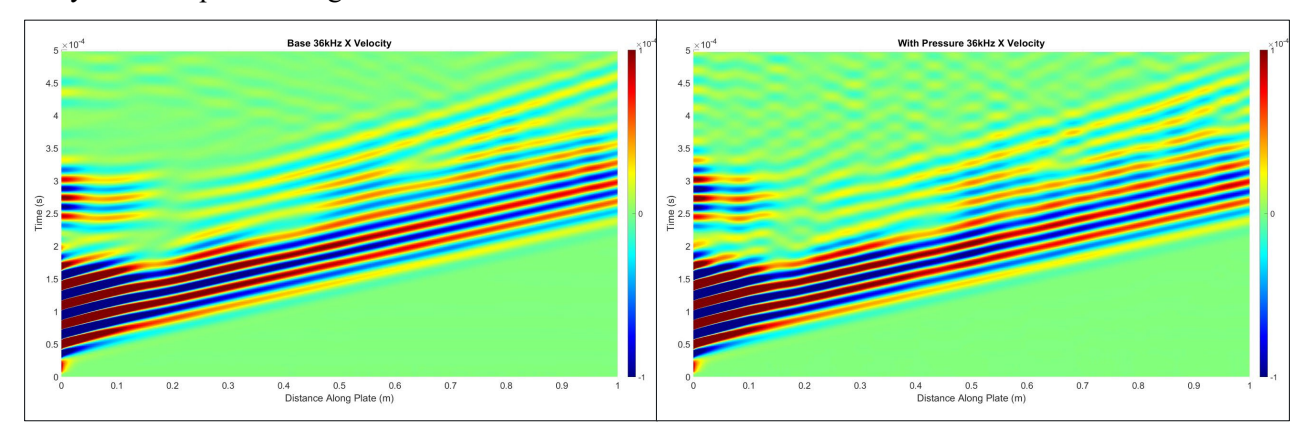


Figure A.8. Spatial-Time Wave Propagation History: X Component of Velocity

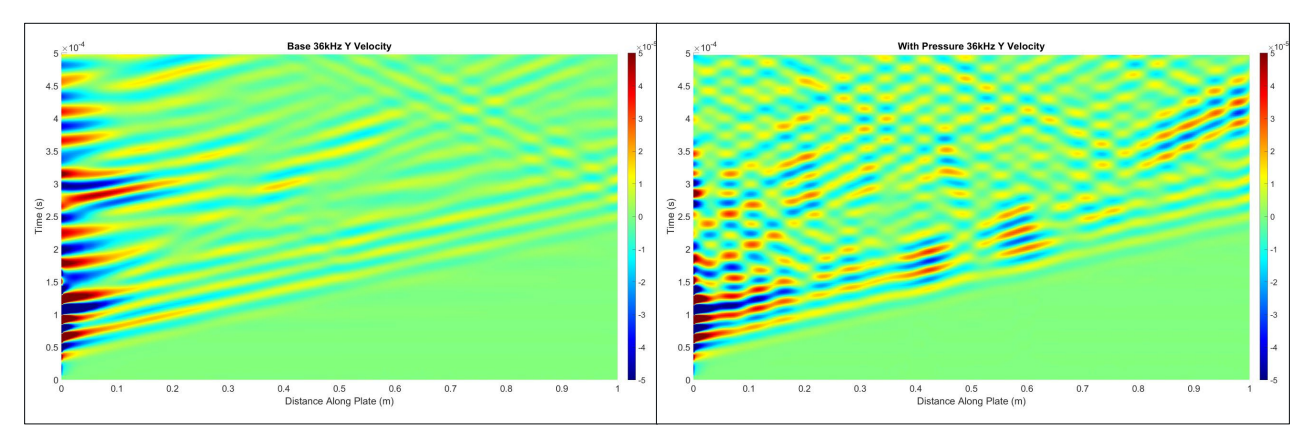


Figure A.9. Spatial-Time Wave Propagation History: Y Component of Velocity

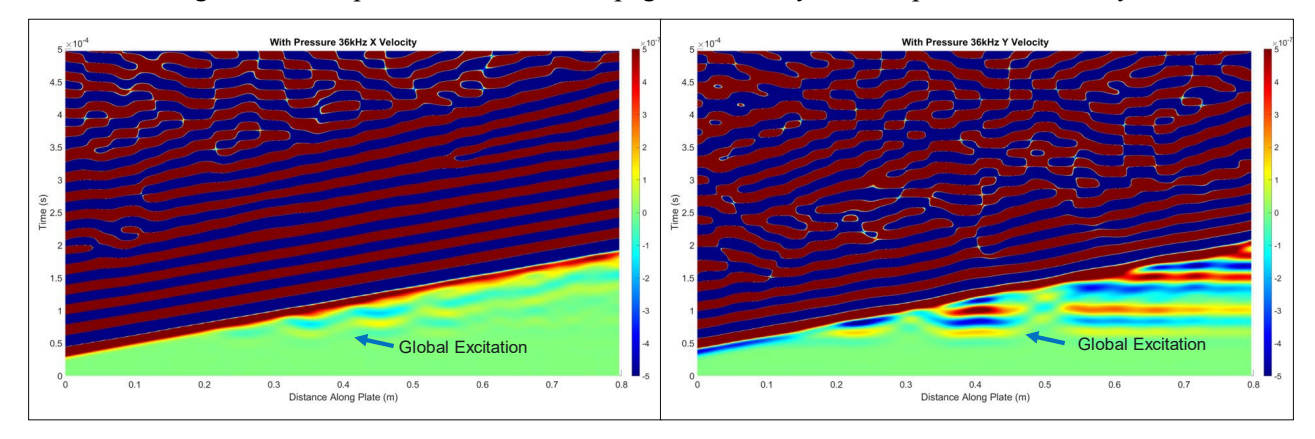


Figure A.10. Spatial-Time Wave Propagation History: Global Excitation of Applied Pressure Region